



Ti^{3+} self-doped TiO_2 nanotubes photoelectrode decorated with Ar- Fe_2O_3 derived from MIL-100(Fe): Enhanced photo-electrocatalytic performance for antibiotic degradation

Meiyng Jia ^{a,b}, Qi Liu ^{a,b}, Weiping Xiong ^{a,b,*}, Zhaohui Yang ^{a,b,*}, Chang Zhang ^{a,b}, Dongbo Wang ^{a,b}, Yinping Xiang ^{a,b}, Haihao Peng ^{a,b}, Jing Tong ^{a,b}, Jiao Cao ^c, Haiyin Xu ^d

^a College of Environmental Science and Engineering, Hunan University, Changsha 410082, PR China

^b Key Laboratory of Environmental Biology and Pollution Control (Hunan University), Ministry of Education, Changsha 410082, PR China

^c School of Hydraulic and Environmental Engineering, Changsha University of Science & Technology, Changsha 410114, PR China

^d College of Environmental Science and Engineering, Central South University of Forestry and Technology, Changsha 410004, PR China



ARTICLE INFO

Keywords:

Ti^{3+} self-doping
Electrodeposition
Photo-electrocatalysis
Metal organic frameworks
 TiO_2 nanotubes

ABSTRACT

The low interfacial mass transfer efficiency between metal-organic framework (MOFs) and conductive substrates makes the development of MOFs-based photoelectrodes challenging. Herein, Ar- Fe_2O_3 / Ti^{3+} - TiO_2 -NTs photoelectrodes are obtained through electrochemical reduction, pulsed deposition, MOFs self-assembly, and sculptural reduction processes. The target photoelectrodes achieve 100% degradation of tetracycline (TC) within 90 min, and the photo-electrocatalytic synergy factor is estimated to be 4.20. Ar- Fe_2O_3 / Ti^{3+} - TiO_2 -NTs photoelectrodes also exhibit excellently in multiple antibiotics and real samples. The reduction self-doping of Ti^{3+} retains vertical orientation properties of nanotubes to provide a path for electronics, and heightens the light-harvesting capacity. The pulse deposition improves the dispersibility of Fe, which is beneficial to the self-assembly of MIL-100(Fe). After sculpture-reduction processes, Ar- Fe_2O_3 retains the porous structure of MIL-100(Fe), and the heterojunction formed with Ti^{3+} - TiO_2 -NTs can significantly enhance the interface charge transfer. This work enriches the electrochemical modification strategy of TiO_2 -NTs, and gives new insights into the development of MOFs-based photoelectrodes.

1. Introduction

Recently, the demand for metal organic frameworks (MOFs) to participate in various reactions in a non-powder state to avoid the difficulty of catalyst recovery has been imminent. For example, the aerogel state participates in the adsorption, the biochar loaded state participates in the persulfate activation, etc. [1,2]. However, the above strategies cannot precisely control the dispersion of MOFs in the load base. Considering the easy recombination of photo-electrons and holes (e^- - h^+) of MOFs in photocatalysis, it seems feasible to utilize MOFs in the form of photoelectrodes to remove recalcitrant organic chemical pollutants and simultaneously achieve effective separation of e^- - h^+ pairs. In this strategy, a potential gradient can be generated inside the photoelectrode by applying a certain anode bias to force the e^- to move towards the counter electrode, and the photogenerated carriers can be effectively separated [3]. However, the study of MOFs in photo-electrocatalytic

degradation for organic pollutants is extremely limited. Furthermore, most of the current research is to coat MOFs powder on conductive substrate to form electrodes, which would decrease the mass transfer rate between MOFs and conductive substrate. In order to solve the above problems, it is necessary to find a matrix with a unique structure to realize the effective combination with MOFs for photo-electrocatalysis (PEC).

Titanium dioxide (TiO_2), as a semiconductor metal oxide, has a rich research foundation in the past few decades. Among the many forms, the TiO_2 nanotubes (TiO_2 -NTs) structure with corrosion resistance and large specific surface area, is considered as a matrix for PEC due to the geometric, electrical and optical properties [4]. The TiO_2 -NTs prepared by the traditional alkaline hydrothermal method are usually arranged disorderly, and the diameter of the tube is small, which causes the inner surface of the nanotubes unusable and electroactive materials could seldom enter into the nanotubes [5]. TiO_2 -NTs prepared by

* Corresponding authors at: College of Environmental Science and Engineering, Hunan University, Changsha 410082, PR China.

E-mail addresses: xiongweiping@hnu.edu.cn (W. Xiong), yzh@hnu.edu (Z. Yang).

electrochemical anodization method can precisely control the structural parameters of nanotubes (such as pore size, wall thickness and length) by adjusting the oxidation conditions, which provides a more accessible space for the reaction and promotes the fullness of electroactive materials [6,7]. In addition, the ordered and tightly arranged nanotubes not only provide a solid support structure to allow the specified electroactive material load, but also reduce the light reflection loss due to multiple radiation scattering from the wall [8]. At present, well-aligned TiO₂-NTs prepared by electrochemical anodic oxidation have been proven to be promising photoanodes for water purification [9,10], hydrogen production [11], and antimicrobial [12].

However, TiO₂-NTs cannot be regarded as an ideal photoelectrode matrix due to the low utilization of visible light caused by the large band gap. The effective ways to overcome the obstacle are to use non-metal doping, transition metal sensitization or coupling with a narrow band gap semiconductor to inject photo-generated electrons into the conduction band (CB) of TiO₂. Because of the transition metal centers and semiconductor-like properties, MOFs just meet the proposed strategy. Therefore, in our previous work, we grew ZIF-8 in situ on the surface of TiO₂-NTs photosensitized by co-doping with N and F [13]. The obtained photoelectrode could effectively improve the visible light of visible light and the separation of carriers to achieve effective degradation. However, heterogeneous doping is usually accompanied by the generation of impurity levels in the band gap, which may reduce the catalytic activity via acting as a recombination center of carriers. Therefore, it is necessary to choose a more suitable way to realize the photosensitization of TiO₂-NTs. Studies have achieved partial reduction of Ti⁴⁺ in powdered TiO₂ by constructing a reducing atmosphere, which confirmed the contribution of Ti³⁺ self-doping to the photosensitization of TiO₂ [14]. However, how to effectively realize the Ti³⁺ self-doping of nanotubes is still a problem. In addition, the low dispersion of MOFs on nanotubes and the weak bond contact with semiconductors matrix also limit the visible light response and charge separation of the photoelectrode. Therefore, it is necessary to choose a more effective method to improve the dispersion and compactness of MOFs on TiO₂-NTs.

Herein, in response to the above problems, we first prepared Ti³⁺ self-doped TiO₂-NTs by electrochemical reduction, which not only realized the photosensitization of the nanotubes, but also improved the conductivity of the pores bottom. Furthermore, Fe metal centers were deposited into the nanotubes by pulse deposition. After self-assembly of MIL-100(Fe) and further calcination under argon, Ar-Fe₂O₃/Ti³⁺-TiO₂-NTs photoelectrode was obtained. The internal structure, surface morphology, element valence, and photoelectrochemical properties of the photoelectrode were detailedly characterized. The improvement of photostability and charge transfer were confirmed by long-term photocurrent decay curve and carrier density analysis, respectively. For evaluating the catalytic performance of Ar-Fe₂O₃/Ti³⁺-TiO₂-NTs photoelectrode, we selected tetracycline (TC), which is the second most common antibiotic in human and animal therapy [15], as the target pollutant. Because tetracycline with persistence and stability is difficult to be completely metabolized in organisms after being widely used in human, poultry and fish farming, resulting in its frequent detection in water cycling system, posing a threat to human health and ecosystem balance [16,17]. Besides, TC can induce many drug-resistant genes and drug-resistant bacteria, which has a great ecological risk [18]. In addition to tetracycline, the catalytic performance of the Ar-Fe₂O₃/Ti³⁺-TiO₂-NTs photoelectrode was also evaluated in real samples and multiple antibiotics. Finally, a possible photo-electrocatalytic degradation mechanism was suggested based on the Tauc plots, band gap energy, valence band spectrum, Mott-Schottky curve and quenching experiment analysis.

2. Experimental section

2.1. Preparation of Ar-Fe₂O₃/Ti³⁺-TiO₂-NTs

Titanium foil ($3.5 \times 3.5 \text{ cm}^2$) were polished and ultrasonically cleaned with acetone, ethanol and ultrapure water for 15 min, respectively. Then the pretreated titanium foil were prepared by anodic oxidation and crystallization to form anatase TiO₂-NTs (Fig. S1), as described in our previous work [13]. According to the cyclic voltammetry curve (Fig. S2a), Ti³⁺-TiO₂-NTs were electrochemically reduced in 0.1 M Na₂SO₄ solution with a cathode voltage of -1.3 V for 20 min via the CHI 660E electrochemical workstation (Fig. S2b). Before electrochemical deposition, in order to further enlarge the resistance difference between the bottom and top of the nanotubes, a voltage of -1.5 V was applied with 1 M (NH₄)₂SO₄ solution and maintained for 3 s (Fig. S2c).

Electrodeposition of Fe was carried out after the bottom of the tube was converted into a highly conductive state and the tube wall was kept in a low conductive state. Specifically, multi-current steps method was utilized with the help of the CHI 660E workstation, which consisted of switching between the cathode pulse (0.25 A, 10 ms) and anode pulse (0.25 A, 3 ms) at room temperature to obtain Fe-Ti³⁺-TiO₂-NTs after 300 cycles (Fig. S2d). The self-assembly process was completed after the Fe-Ti³⁺-TiO₂-NTs was immersed in a mixture of N-N dimethylformamide (DMF), Benzene-1,3,5-tricarboxylic acid (H₃BTC, 98%), nitric acid (HNO₃) and hydrofluoric acid (HF) at 150 for 24 h. After washing and drying in ethanol, the self-assembled photoelectrode was treated in argon at 450 °C for 2 h to complete the conversion of MIL-100(Fe)/Ti³⁺-TiO₂-NTs to Ar-Fe₂O₃/Ti³⁺-TiO₂-NTs (Scheme 1).

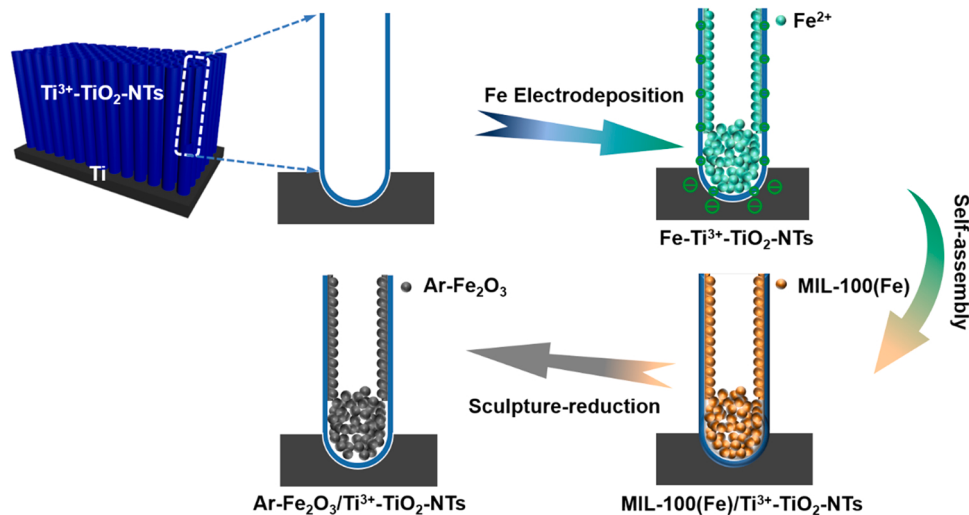
2.2. The photo-electrocatalytic experiments

The photo-electrocatalytic activity of Ar-Fe₂O₃/Ti³⁺-TiO₂-NTs photoelectrode was assessed by the degradation of Tetracycline (TC) in a three-electrode quartz cell (250 mL) with Na₂SO₄ (0.05 M) as the electrolyte. After 30 min in darkness to achieve the adsorption-desorption balance of TC (20 mg·L⁻¹) on the photoelectrode, a light source was set up at a certain distance from the photoelectrode for photo-electrocatalytic degradation. At each irradiation time intervals, 1.5 mL of samples were gathered for high-performance liquid chromatography (HPLC) analysis. The reproducibility was checked by repeating the results at least 3 times and found to be within an acceptable range. The intermediates of TC were identified by Liquid chromatography-mass spectrometry (Agilent Technologies, 6470 Triple Quad LC-MS). The specific analysis operation of HPLC and LC-MS was demonstrated in Supporting Information.

3. Results and discussion

3.1. Characterization of catalyst

X-ray diffraction (XRD) of photoelectrodes was shown in Fig. 1a. TiO₂-NTs with anatase (101) facets was obviously confirmed (JCPDS card 21-1272), and the peak at 25.3° could be noticed in all film electrodes. The reduced Ti³⁺-TiO₂-NTs electrodes retained the typical crystal peaks of TiO₂-NTs, which was consistent with our previous research [14]. After electrodeposition, the XRD of 35.63° could be easily observed, indicating the successful deposition of Fe on Ti³⁺-TiO₂-NTs electrodes (JCPDS card 39-1346). The XRD patterns of MIL-100(Fe)/Ti³⁺-TiO₂-NTs electrodes exhibited the unique peaks, which were ascribed to both Ti³⁺-TiO₂-NTs and MIL-100(Fe) (e.g., 20=11°, 37.8°, 48.1°) [19,20]. Markedly, MIL-100(Fe) displayed a relatively weak characteristic peak, which could be attributed to the limited loading. Subsequently, the characteristic peak of MIL-100(Fe) was lost after sculpture-reduction processes in argon atmosphere. Meanwhile, the intensity of crystal peak at 35.63° increased significantly, which proved



Scheme 1. The preparation of Ar- Fe_2O_3 /Ti³⁺- TiO_2 -NTs photoelectrode (Take a single nanotube as an example).

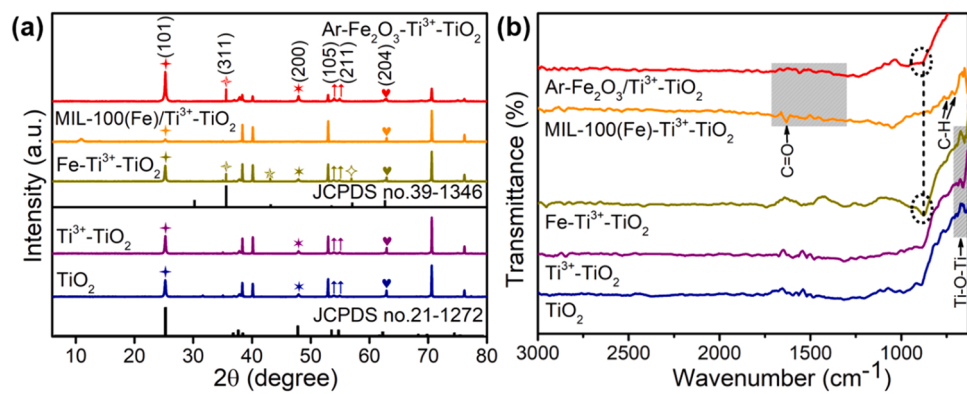


Fig. 1. (a) XRD patterns; (b) FTIR spectra of TiO_2 , $\text{Ti}^{3+}\text{-}\text{TiO}_2$, $\text{Fe}\text{-}\text{Ti}^{3+}\text{-}\text{TiO}_2$, $\text{MIL-100(Fe)}\text{-}\text{Ti}^{3+}\text{-}\text{TiO}_2$ and $\text{Ar-}\text{Fe}_2\text{O}_3\text{/Ti}^{3+}\text{-}\text{TiO}_2$.

the successful evolution of Fe_2O_3 magnetic phase from the crystalline MIL-100(Fe). Finally, the XRD pattern of Ar- Fe_2O_3 /Ti³⁺- TiO_2 -NTs film electrodes confirmed the successful deposition of Fe and the self-assembly of MIL-100(Fe).

Fourier transform infrared (FTIR) spectrum was applied to identify the surface chemical bonds of film electrodes (Fig. 1b). For pure TiO_2 -NTs, the main peak at 400–700 cm^{-1} was divided into the Ti-O-Ti stretching vibration modes, and the peak at 1650 cm^{-1} was attributed to physically surface-adsorbed water [21]. Compared with TiO_2 -NTs, the chemical structure of anode $\text{Ti}^{3+}\text{-}\text{TiO}_2$ -NTs displayed no obvious change [22]. The FTIR spectrum of MIL-100(Fe) exhibited obvious adsorption of C=O bond at 1628 cm^{-1} originating from carboxylate, and C-H bond at 760 and 707 cm^{-1} deriving from the bending vibration of benzene [23]. In addition, the peak between 1700 and 1300 cm^{-1} was related to the carboxylic acid ligand, which was corresponded to the coordination effect of terephthalic acid with the iron site [24]. Similar to the literature results [14], the characteristic peak of C=O bond weakened after calcination, indicating the damage of carboxylate groups in MIL-100(Fe). For the Ar- Fe_2O_3 /Ti³⁺- TiO_2 -NTs composite electrode, the characteristic peaks of $\text{Ti}^{3+}\text{-}\text{TiO}_2$ -NTs and Ar- Fe_2O_3 (the black circle in Fig. 1b) could be clearly observed, indicating the coexistence of the two.

The microstructure of photoelectrodes were recorded by scanning electron microscope (SEM) (Fig. 2), and the images illustrated that the nanotube arrays was successfully prepared on the surface of the titanium foil. The bare TiO_2 -NTs performed a highly ordered structure and a vertically oriented hollow tube (Fig. 2a). Compared with TiO_2 -NTs, the morphology of $\text{Ti}^{3+}\text{-}\text{TiO}_2$ -NTs was basically unchanged. After

electrochemical deposition of Fe, the $\text{Ti}^{3+}\text{-}\text{TiO}_2$ -NTs matrix was uniformly covered by small and dispersed Fe nanoparticles. Interestingly, Fe grew from the bottom to the wall and surface of the $\text{Ti}^{3+}\text{-}\text{TiO}_2$ -NTs (Fig. S3), without destroying the nanotube structure or finding particle aggregation to block the tube due to the rigid support of TiO_2 -NTs array (Fig. 2b). The self-assembly of MIL-100(Fe) was carried out on the wall of $\text{Ti}^{3+}\text{-}\text{TiO}_2$ -NTs, and most of the nozzles were still retained (Fig. 2c). After calcination, Ar- Fe_2O_3 /Ti³⁺- TiO_2 -NTs maintained a cross-linked porous structure with open channels (Fig. 2d). As could be seen from the enlarged images, due to the formation of the spindle structure (Fig. 2e), a film of 6.926 μm was finally formed on the nanotube surface (Fig. 2f). Therefore, the final open porous structure and well-arranged tubular structure of the film electrode were conducive to the charge transfer at the electrode/electrolyte interface [5].

The transmission electron microscopy (TEM) characterization was adopted to observe the internal structure of Ar- Fe_2O_3 /Ti³⁺- TiO_2 -NTs photoelectrode (Fig. 2g-i). The obvious particles in the compact nanotubes could be observed in Fig. 2h. Combined with the SEM results, we could speculate that this was the result of Fe deposition and the self-assembly of MIL-100 (Fe). The selected area electron diffraction (SAED) inset in Fig. 2h showed the diffraction rings, indicating the polycrystalline nature of Ar- Fe_2O_3 /Ti³⁺- TiO_2 -NTs [25]. The diffraction rings of the (101) and (301) crystal planes could be easily observed, which was consistent with the XRD results (Fig. 1a). The high resolution TEM (HRTEM) images of Ar- Fe_2O_3 /Ti³⁺- TiO_2 -NTs showed typical lattice fringe spacing (0.352, 0.292 and 0.296 nm) in Fig. 2i, which were corresponding to anatase TiO_2 (101), Ti_3O_5 (112) and Fe_2O_3 (311),

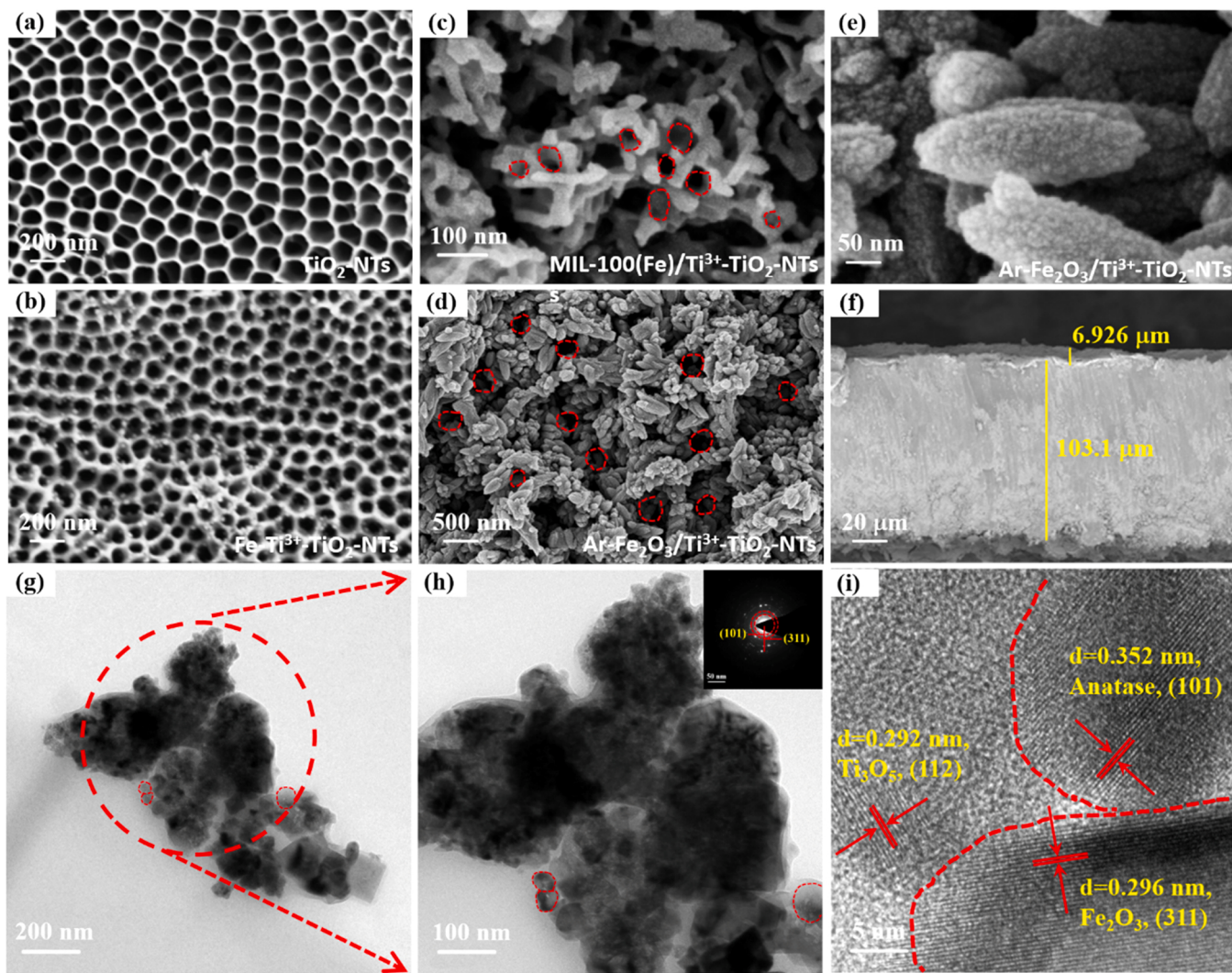


Fig. 2. SEM images of (a) TiO₂-NTs, (b) Fe-Ti³⁺-TiO₂-NTs, (c) MIL-100(Fe)/Ti³⁺-TiO₂-NTs, (d) (e) Ar-Fe₂O₃/Ti³⁺-TiO₂-NTs, (f) Cross-section topography of Ar-Fe₂O₃/Ti³⁺-TiO₂-NTs; (g-i) TEM images of Ar-Fe₂O₃/Ti³⁺-TiO₂-NTs; (i) HRTEM of Ar-Fe₂O₃/Ti³⁺-TiO₂-NTs. The inset in (h) shows the SAED pattern of Ar-Fe₂O₃/Ti³⁺-TiO₂-NTs.

respectively [26,27]. According to HRTEM image, Ti₃O₅ (112) and Fe₂O₃ (311) were tightly combined, indicating that Ti³⁺-TiO₂-NTs and Ar-Fe₂O₃ formed a heterojunction. The above analysis proved that the proposed preparation route could realize the good dispersibility of Ar-Fe₂O₃ and excellent tightness with Ti³⁺-TiO₂-NTs.

The surface roughness and morphology of Ti³⁺-TiO₂-NTs, MIL-100(Fe)/Ti³⁺-TiO₂-NTs and Ar-Fe₂O₃/Ti³⁺-TiO₂-NTs were further studied by atomic force microscope (AFM). The three-dimensional height image of the film was shown in Fig. 3, and the roughness parameter was reported in Table 1. The AFM image showed that there were different degrees of depressions on the surface of the film electrode. Compared with Ti³⁺-TiO₂-NTs (Fig. 3a), the observed vertical distortions (vertical roughness) of MIL-100(Fe)/Ti³⁺-TiO₂-NTs was significantly enhanced (Fig. 3b), and Ar-Fe₂O₃/Ti³⁺-TiO₂-NTs performed the roughest surface with 156 nm (Fig. 3c and d). These results revealed that argon calcination opened the mouth of nanotube which was self-assembled by MIL-100(Fe), because only when the diameter of the nanotube became wide enough, the tip could penetrate inside the hollow nanotube interior and displayed different vertical distortions, which was not possible with TiO₂-NTs with a smaller diameter [28]. This conclusion was consistent with the results of SEM (Fig. 2d).

X-ray photoelectron spectroscopy (XPS) was carried out to analyze elemental composition and chemical state. The scan spectrum of Ar-

Fe₂O₃/Ti³⁺-TiO₂-NTs at low resolution was shown in Fig. 4a, and Fe, O, Ti and C could be detected in target electrode. Compared with TiO₂-NTs, the typical peak pair of Ti⁴⁺ in Ti³⁺-TiO₂-NTs exhibited a slight negative shift (Fig. 4b) [29]. Concomitantly, additional peak pairs appeared at 456.90 eV (Ti³⁺ 2p3/2) and 463.30 eV (Ti³⁺ 2p1/2), which was related to the change of the bonding environment during the reduction process, indicating that both Ti⁴⁺ and Ti³⁺ were present in the target electrode. After curve fitting of the Fe2p spectrum in MIL-100(Fe)/Ti³⁺-TiO₂-NTs, four binding energy peaks could be observed at 728.8, 724.9, 714.6 and 711.6 eV, corresponding to Fe³⁺ 2p1/2, Fe²⁺ 2p1/2, Fe³⁺ 2p3/2 and Fe²⁺ 2p3/2, indicating the coexistence of Fe²⁺ and Fe³⁺ [30]. Remarkably, both the peak at 719.4 eV and above peak of Ar-Fe₂O₃/Ti³⁺-TiO₂-NTs showed a negative shift (Fig. 4c). For the O1s peak (Fig. 4d), the O1s spectrum of MIL-100(Fe)/TiO₂-NTs exhibited peaks at 530.4 eV and 532.0 eV, which were lattice oxygen (Ti-O/Fe-O) and the chemically adsorbed oxygen (such as -OH, -CO) [27]. In Ar-Fe₂O₃/Ti³⁺-TiO₂-NTs, in addition to the two main peaks shifting negatively, a third signal peak was also observed at 532.5 eV, indicating that the electrochemical reduction caused oxygen vacancies [31]. Meanwhile, the lattice oxygen performed a higher peak area than that of MIL-100(Fe)/TiO₂-NTs, indicating that more Ti-O/Fe-O exposed after high-temperature calcination and shared lattice electrons, thereby obtaining a larger fraction of the oxygen-deficient area [32]. The above

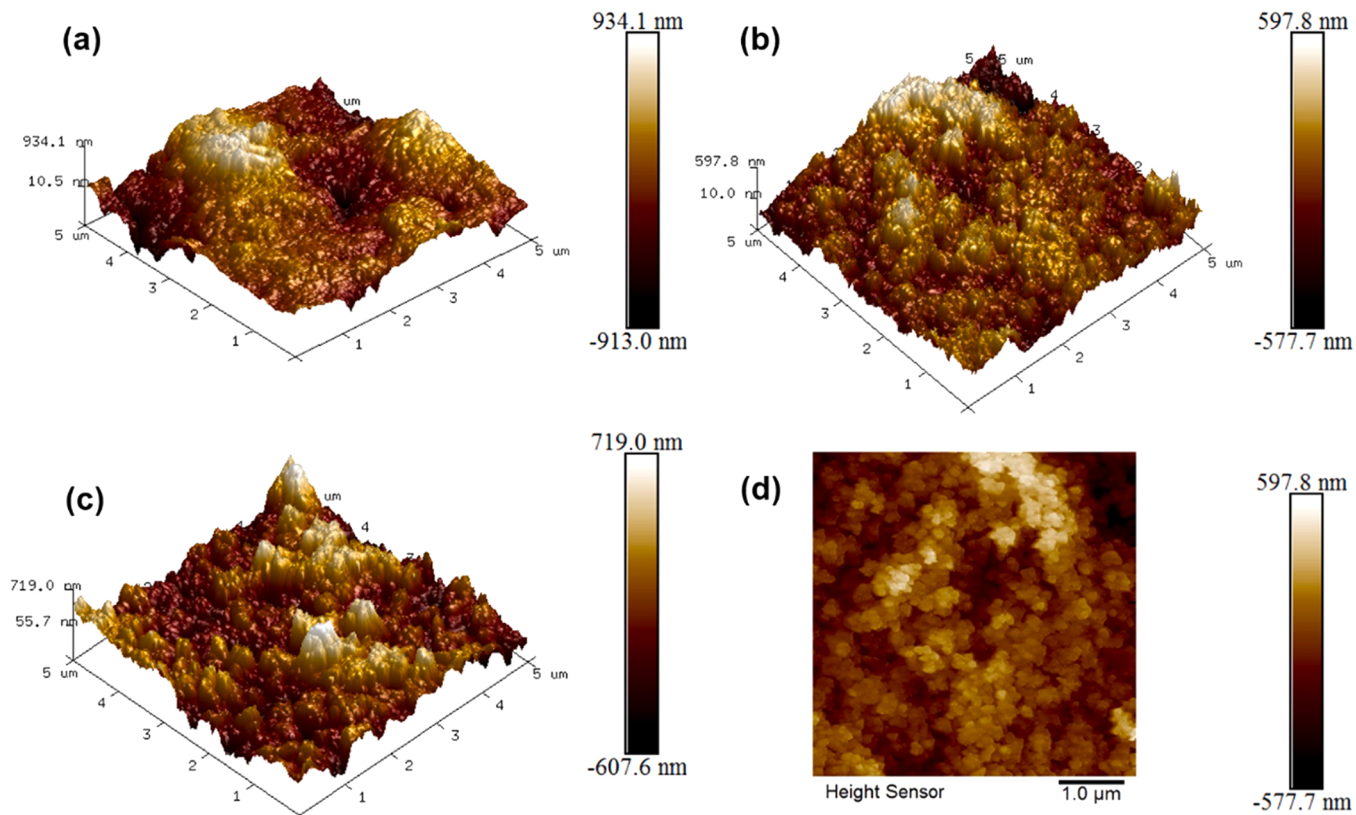


Fig. 3. 3-Dimensional height images of (a) Ti³⁺-TiO₂-NTs, (b) MIL-100(Fe)/Ti³⁺-TiO₂-NTs, (c) Ar-Fe₂O₃/Ti³⁺-TiO₂-NTs; (d) micrographs of Ar-Fe₂O₃/Ti³⁺-TiO₂-NTs.

Table 1
Values of roughness parameter obtained from AFM measurements.

| Sample | Rq (RMS roughness) | Ra (average roughness) |
|--|--------------------|------------------------|
| Ti ³⁺ -TiO ₂ -NTs | 150 nm | 113 nm |
| MIL-100(Fe)/Ti ³⁺ -TiO ₂ -NTs | 157 nm | 123 nm |
| Ar-Fe ₂ O ₃ /Ti ³⁺ -TiO ₂ -NTs | 196 nm | 156 nm |

results confirmed the synergistic promotion between the formation of oxygen vacancies by electrochemical reduction and calcination in an inert atmosphere.

3.2. Optical property and photo-electrochemistry characteristics

UV-vis diffuse reflectance spectrum (UV-vis DRS) was introduced to evaluate the optical properties and band gap energies of the film electrodes. TiO₂-NTs could only absorb light below 400 nm due to the wide band gap. After reduction, the absorption edge of the Ti³⁺-TiO₂-NTs electrode extended to the visible light region, and exhibited a significantly enhanced visible light absorption in the range of 436–700 nm. After the electro-deposition of Fe and the completion of self-assembly, MIL-100(Fe)/Ti³⁺-TiO₂-NTs performed excellent visible light absorption ability through the sensitization of MIL-100(Fe), and was maintained after calcination under argon (Fig. 5a). The above results verified that electrochemical reduction and Ar-Fe₂O₃ sensitization derived from MIL-100(Fe) could effectively improve the light absorption performance of TiO₂-NTs. The improved light absorption ability beneficial to more photo-carriers being utilized by the photoelectrode, generating more active radicals and improving the photoelectrocatalytic performance. The Tauc diagram transformed by the Kubelka-Munk method (Eq. (1), n = 1 for direct transition and n = 4 for indirect transition) can estimated the band gap of the photoelectrodes [21]. Since the conductive substrate TiO₂ is a direct semiconductor [33], the band gap of the

photoelectrodes are estimated by the plot of $(\alpha h\nu)^{1/2}$ as a function of photon energy ($h\nu$). Accordingly, the band gap of Ti³⁺-TiO₂-NTs was shortened by 2.80 eV from 3.08 eV of TiO₂-NTs, and the final band gap of Ar-Fe₂O₃/Ti³⁺-TiO₂-NTs was 2.63 eV (Fig. 5b).

$$\alpha h\nu = A(h\nu - E_g)^n/2 \quad (1)$$

In addition to the light-harvesting capacity, the photo-generated carrier separation characteristics are also an significant factor involving the performance of PEC. Therefore, the photophysical behavior of the photoelectrodes were further studied by photoluminescence (PL). Generally speaking, a decrease in PL intensity means a decrease in the recombination rate of photogenerated carriers and an increase in photo-electrocatalytic activity [34]. The emission peak pattern of the reduced Ti³⁺-TiO₂-NTs was slightly different from that of TiO₂-NTs. After deposition, self-assembly and high-temperature calcination, Ar-Fe₂O₃/Ti³⁺-TiO₂-NTs exhibited similar emission peak patterns with Ti³⁺-TiO₂-NTs, but the intensity was continuously reduced (Fig. 5c). Electron transfer to adjacent oxygen vacancies and strong interactions between Ti³⁺-TiO₂ and Ar-Fe₂O₃ lead to possible charge transfer paths that facilitate e⁻-h⁺ separation. Accordingly, Ar-Fe₂O₃/Ti³⁺-TiO₂-NTs performed the best photo-electrocatalytic performance, which also verified the XPS analysis results of oxygen vacancies and negative shifts of characteristic peaks (Fig. 4).

The influence of modified film electrodes on the photo-electrochemical performance is complex, which is usually reflected in the changes of crystallinity and the increase of carrier concentration. Therefore, it was necessary to further measured the Mott-Schottky (M-S) curve to evaluate changes in carrier concentration. The film electrode performed a linear behavior on the M-S plots from –0.7–0.3 V, and exhibited a positive slope, indicating that the photoelectrodes was n-type (Fig. 5d). Notably, the linear behavior of Ti³⁺-TiO₂-NTs was found to deviate at 0.1 V, indicating that there were electronic active surface states in the semiconductor substrate [35]. In addition, the flat band

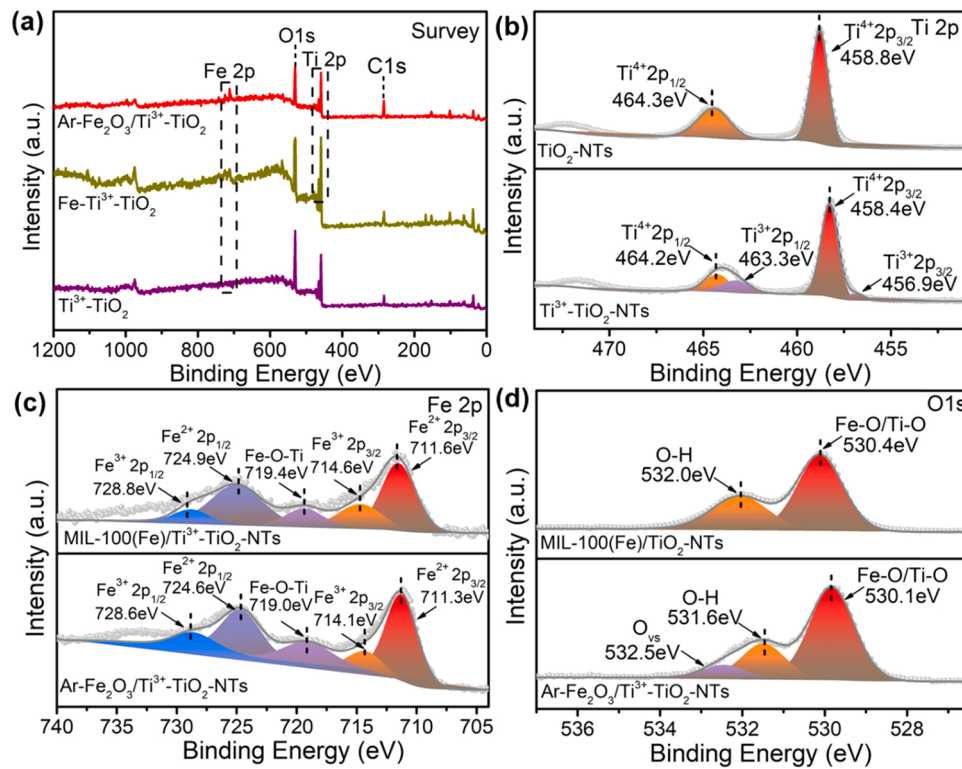


Fig. 4. (a) XPS spectra of Ti^{3+} - TiO_2 -NTs, $\text{Fe}-\text{Ti}^{3+}$ - TiO_2 -NTs and $\text{Ar}-\text{Fe}_2\text{O}_3/\text{Ti}^{3+}$ - TiO_2 -NTs; typical elements (b) Ti 2p, (c) Fe 2p and (d) O 1 s.

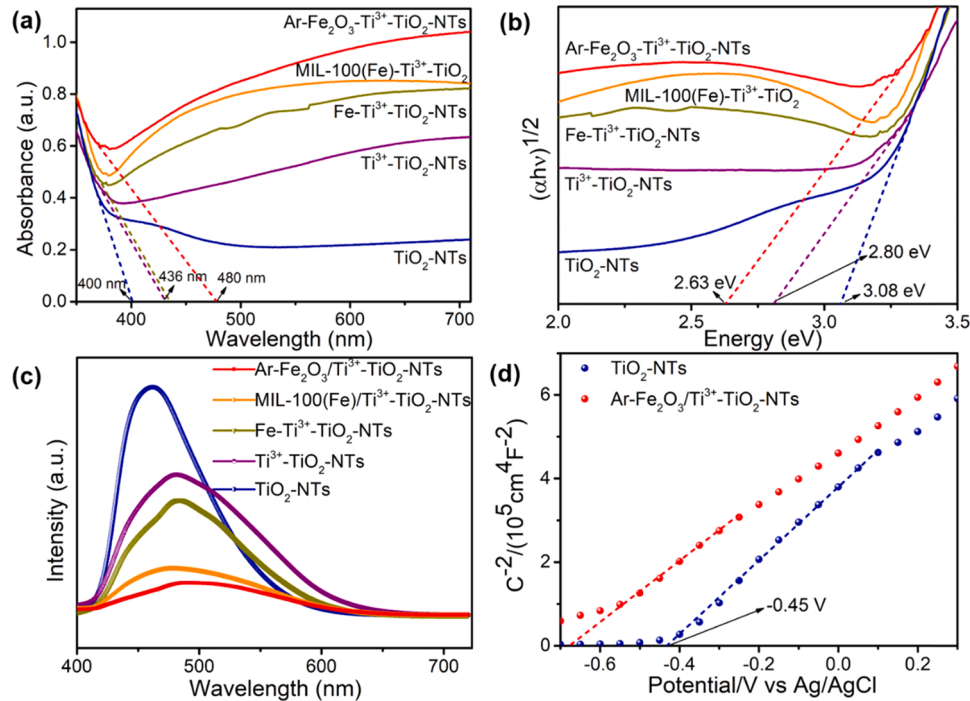


Fig. 5. (a) UV-vis DRS; (b) Tauc plots; (c) PL spectra of TiO_2 -NTs, Ti^{3+} - TiO_2 -NTs, $\text{Fe}-\text{Ti}^{3+}$ - TiO_2 -NTs, $\text{MIL-100(Fe)}/\text{Ti}^{3+}$ - TiO_2 -NTs and $\text{Ar}-\text{Fe}_2\text{O}_3/\text{Ti}^{3+}$ - TiO_2 -NTs; (d) the M-S plots for TiO_2 -NTs and $\text{Ar}-\text{Fe}_2\text{O}_3/\text{Ti}^{3+}$ - TiO_2 -NTs.

potential could be evaluated by extrapolating the linear region in the M-S diagram, and further for calculating the carrier concentration via the Mott-Schottky equation (Eq. (2)).

$$\frac{1}{C^2} = \frac{2}{e\epsilon\epsilon_0 N_D} \left[(V - V_{FB}) - \frac{kT}{e} \right] \quad (2)$$

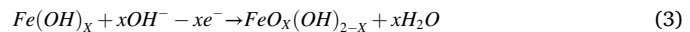
Among them, ϵ , ϵ_0 and k are different constants, namely the dielectric constant, the vacuum permittivity and the Boltzmann constant. C represents the space charge capacitance, N_D represents the donor carrier concentration, V represents the applied potential, V_{FB} is the flat band potential and T is the temperature. The dielectric constant of anatase TiO_2 was 48, and the carrier concentration of TiO_2 -NTs was finally

calculated to be $3.46 \times 10^{22} \text{ cm}^{-3}$. The high carrier concentration could reduce the resistivity of the film, resulting in an increase in incident photon-current efficiency [36]. According to Eq. (2), for the same semiconductor substrate, the smaller the flat-band potential (V_{FB}), the lower the slope of the Mott-Schottky curve (k) and the higher the carrier concentration (N_D). Therefore, the carrier concentration of Ar-Fe₂O₃/Ti³⁺-TiO₂-NTs was higher than that of TiO₂-NTs, and it could be speculated that the photocurrent density of Ar-Fe₂O₃/Ti³⁺-TiO₂-NTs might increase due to the increase of carrier concentration.

The photoresponsivity of photoelectrode under visible light intermittent irradiation was measured by potentiostatic technique. As shown in Fig. 6a, the photocurrent density of the photoelectrode exhibited close correlation related to the on/off cycle. Especially, compared with Fe-Ti³⁺-TiO₂-NTs and MIL-100(Fe)/Ti³⁺-TiO₂-NTs, the photocurrent of Ar-Fe₂O₃/Ti³⁺-TiO₂-NTs was more stable and there was no decay period, indicating that the heterojunction effectively inhibited the photo-electron (e^-) backflow from the CB of Ti³⁺-TiO₂-NTs to Ar-Fe₂O₃ [11]. And the photocurrent density of Ar-Fe₂O₃/Ti³⁺-TiO₂-NTs was the highest, which was 4.6 times of TiO₂-NTs. The higher photocurrent density meant that photo-generated carriers were more efficiently transferred from the photoanode to the counter electrode through the external circuit. These results confirmed the conclusion of the above PL analysis (Fig. 5d).

In addition, EIS Nyquist plots were used to further evaluate the interface charge transfer capability of the photoelectrodes. Except for TiO₂-NTs, the semicircles of other photoelectrodes in the entire frequency range were depressed (Fig. 6b), indicating that the composite electrodes predominantly conducted electrochemical processes controlled by kinetics [5]. Especially, the semicircular of Fe-Ti³⁺-TiO₂-NTs was depressed more obviously, revealing that the strong interaction between Fe and Ti greatly increased the conductivity and the current-carrying electron concentration in the CB [37]. The impedance of the electrode mainly depended on the charge transfer resistance between electrolyte and electroactive material [13]. Therefore, the minimum arc diameter of Ar-Fe₂O₃/Ti³⁺-TiO₂-NTs indicated that a more effective separation of photogenerated e^- - h^+ pairs and faster interfacial charge transfer.

Fig. 6c-d showed the cyclic voltammetry (CV) curves of the photoelectrodes in different modification stages. Among them, TiO₂-NTs, Ti³⁺-TiO₂-NTs, Ar-Fe₂O₃/Ti³⁺-TiO₂-NTs displayed typical cyclic voltammograms, with pronounced peaks during forward and reverse of the scan (Fig. 6c). With the progress of photoelectrode modification, the peak value of anode current gradually increased. Notably, two reduction waves at -0.003 and -0.817 V appeared during the reverse scan of Fe-Ti³⁺-TiO₂-NTs (Fig. 6d), which might be related to the reduction of Fe^{2+} and Fe^{3+} in $\text{FeO}_x(\text{OH})_{2-x}$ to Fe(OH) [5], and the reaction was shown in Eq. (3). After self-assembly, the reduction wave disappeared, and the accompanying increase in oxygen evolution potential effectively avoided the occurrence of additional reaction. The above results confirmed the deposition of Fe through the appearance of the reduction wave and further confirmed the self-assembly of MIL-100(Fe) through the disappearance of the reduction wave.



3.3. Photocatalytic performance

TC was chosen as the target pollutant to evaluate the potential of the photoelectrode in PEC, and the degradation efficiency (DE, %) was calculated by the Eq. (4). Firstly, before electrochemical modification, around 15.35% removal efficiency was achieved via TiO₂-NTs film electrodes (Fig. S4a), which might be attributed to the utilization of trace visible light and the oxidation of dissolved oxygen. After modification, the kinetic fitting (Eq. (5)) displayed that the first-order kinetic constant of the Ar-Fe₂O₃/Ti³⁺-TiO₂-NTs photoelectrode was increased by 21.7 times (Fig. S4b). Then, the photoelectric synergy of film photoelectrodes was further investigated. As shown in Fig. S4c, compared with the degradation efficiencies of PC (24.87%) and EC (57.76%), the PEC performed a significant synergistic effect, which could achieve 100% degradation efficiency in 90 min. In addition, the synergy factor (SF) (Eq. (6)) was evaluated to be 4.20 according to the first-order kinetic constant (k) (Fig. S4d), where k_{PEC} , k_{PC} , and k_{EC} was the first-order kinetic constants in PEC, PC, and EC, respectively [38]. Notably, the photo-electrocatalytic activity of Ar-Fe₂O₃/Ti³⁺-TiO₂-NTs

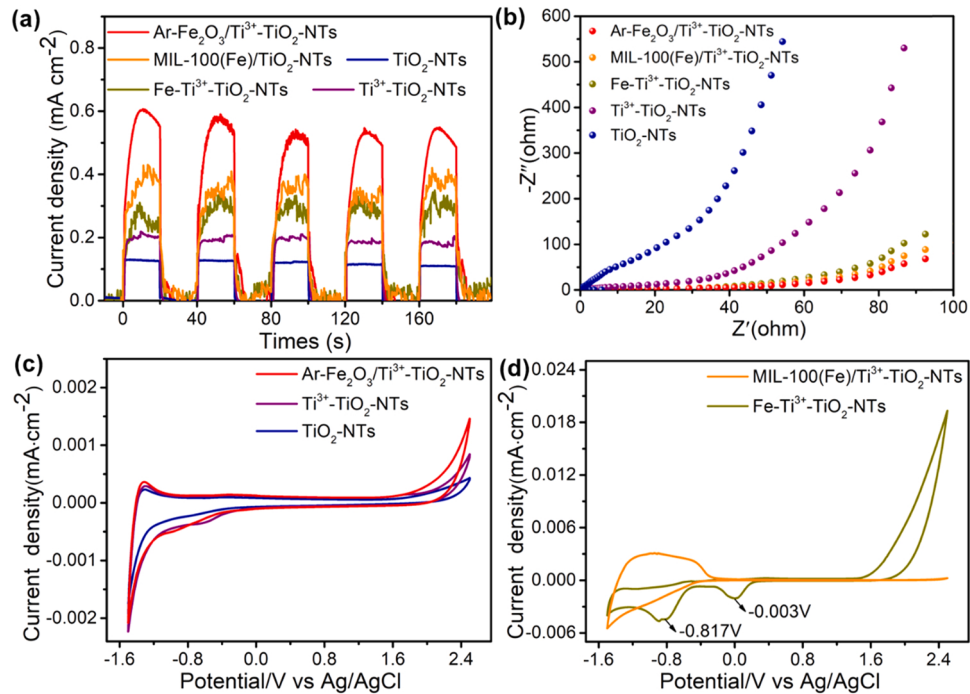


Fig. 6. (a) Photocurrent density (2.0 V vs. Ag/AgCl); (b) EIS Nyquist plots with frequency of 1 kHz; (c) (d) CV images of TiO₂-NTs, Ti³⁺-TiO₂-NTs, Fe-Ti³⁺-TiO₂-NTs, MIL-100(Fe)/Ti³⁺-TiO₂-NTs and Ar-Fe₂O₃/Ti³⁺-TiO₂-NTs. Experimental conditions: scan rate = 50 mV·s⁻¹.

photoelectrode was higher than other TiO₂-based photoelectrodes (Table 2).

Considering the adsorption performance of the photoelectrode, N₂ adsorption-desorption isotherm of TiO₂-NTs, Ti³⁺-TiO₂-NTs, Fe-Ti³⁺-TiO₂-NTs, MIL-100(Fe)/Ti³⁺-TiO₂-NTs, and Ar-Fe₂O₃/Ti³⁺-TiO₂-NTs were characterized (Fig. S5). The relevant statements and physicochemical parameters (Tab. S1) were provided in the Supporting Information.

$$DE\% = (1 - C_t/C_0) \times 100\% \quad (4)$$

$$k = \ln(C_0/C_t)/t \quad (5)$$

$$SF = \frac{k_{PEC}}{k_{PEC} + k_{EC}} \quad (6)$$

The applied voltage is an important factor that affects the photoelectrochemical catalytic performance. Before determining other optimal conditions, the most suitable voltage within the applicable range should be considered firstly. Fig. 7a and b displayed that the reaction rate increased from 0.0337 min⁻¹ to 0.0780 min⁻¹ with the applied voltage increased from 0.5 V to 2.5 V, which might be because voltage could not only improve the electron transfer rate of pollutants to the photoelectrode, but also enhance the ability of hydroxyl radical (•OH) formation on the photoelectrode surface [45]. After 90 min degradation, the TC removal efficiencies of thin film electrodes reached 88.66%, 92.06%, 94.56%, 100% and 100% at 0.5, 1.0, 1.5, 2.0 and 2.5 V, respectively. Notably, the effect of the applied voltage on the final degradation efficiency was not particularly obvious, especially when the applied voltage was increased from 2.0 V to 2.5 V, the degradation efficiency could both reach 100%. Therefore, the effect of applied voltage was mainly reflected in the increase of electron transfer rate rather than the generation of •OH in this study, and the production of •OH might perform little effect on PEC. Considering that additional reaction such as oxygen evolution were likely to occur under higher applied voltage, 2.0 V was determined as the most suitable applied voltage.

In practical applications, different water systems such as wastewater and surface water have different pH values. Therefore, it is necessary to evaluate the effect of the initial pH value on the photo-electrocatalytic process. The effect of initial pH values ranging from 2 to 10 on TC degradation was shown in Fig. 7c. The experimental data exhibited that the removal efficiency of TC increased at first and then decreased with increasing pH. When the pH value was 6, the film electrode performed the best reaction rate of 0.0684 min⁻¹ and the degradation efficiency of 100% for TC (Fig. 7d). Compared with low pH, high pH was more conducive to the degradation of TC. This was related to the characteristic that TC was sensitive to pH value of the solution due to the protonation state [46]. TC molecules existed in three different forms in aqueous solutions with different pH values, including cationic species (pH<3.3), zwitterionic form (3.3<pH<7.7) and anionic species (pH>7.7) [47]. Under neutral or alkaline conditions, TC molecules existed in zwitterionic or anionic species, which was more conducive to the adsorption on the surface of the photoanode and further

photoelectrocatalytic degradation. While electrolyte would be consumed excessively when the solution was too alkaline. The conductivity of the solution would reduce due to the lack of electrolyte, thus performing a slightly reduced reaction rate and degradation efficiency [48].

Fig. 7e displayed the degradation efficiency-time curve of TC for thin film photo-electrodes prepared with different electrodeposition times. When the electrodeposition time was relatively short (1 min), the corresponding degradation efficiency of the system for TC was only 42.01%. When the deposition time was further increased to 3 min, the degradation efficiency was significantly improved (94.08%). When the deposition time was short, the self-assembly of MIL-100(Fe) might not occur due to less Fe deposited and thus affecting the degradation efficiency. 5 min seemed to be the optimum time for electrodeposition. When the deposition time was extended to 7 min, the degradation efficiency decreased, which might due to the agglomeration and loss of active sites caused by excessive deposits [49].

Photon flux from the radiation source is another important factor in PEC. Studies have shown that the PEC efficiency increased linearly with the photon flux or the square root of the photon flux, but related research was currently limited. In order to study the effect of photon flux (light intensities) on the photoelectrocatalytic ability of film electrodes, the distance between photoelectrodes and light source (2, 4, 6, 8 and 10 cm) was changed to control the photon flux. Table 3 summarized the photon flux corresponding to the distance between the photoelectrodes and light source. According to the experimental results (Fig. 7f), when the photon flux was high enough, the final degradation efficiency of TC in the PEC system under different photon fluxes was similar. However, the first-order kinetic constant (k) depended on the photon flux, and the reaction rate under 318.2 mW·cm⁻² ($k = 0.0684 \text{ min}^{-1}$) was significantly better than that under lower photon flux ($k = 0.0138 \text{ min}^{-1}$) (Fig. S6). Considering factors such as experimental equipment and lamp source protection, we set the distance at 6 cm to control the photon flux of 318.2 mW·cm⁻² in subsequent experiments.

3.4. Stability, recyclability and reusability

Electrodes with practical application potential should be excellent in stability, recyclability and reusability. In terms of light stability, the long-term photocurrent decay curve of Ar-Fe₂O₃/Ti³⁺-TiO₂-NTs photoelectrodes had been continuously tested under 2 V (vs Ag/AgCl). As shown in Fig. 8a, the photocurrent-time curve performed no obvious downward trend, demonstrating the superior light stability of photoelectrode. In addition, the water stability of the photoelectrode was proved in a degradation system prepared in different water bodies, and the related parameters were listed in Tab. S2. The film electrodes could maintain high degradation efficiency and rapid degradation for TC in above water bodies (Fig. 8b). Compared with powder catalysts, film electrode performed significantly enhanced recyclability. Therefore, Ar-Fe₂O₃/Ti³⁺-TiO₂-NTs was considered for reusability testing. After five cycles, the removal efficiency of TC hardly decreased and still reached 99.5% (Fig. 8c).

Table 2
Degradation of various pollutants by different TiO₂-based photoelectrodes.

| Photoelectrode | Current Density | k^a/min^{-1} | Pollutants | Removal efficiency | Ref |
|--|---------------------------|-----------------------|---|--------------------|-----------|
| AgBr-Ti ³⁺ /TiO ₂ | 0.025 mA·cm ⁻² | 0.0289 | Methylene blue 5 mg/L, 50 mL | 98.7%–150 min | [39] |
| TiO ₂ -NPs/TiO ₂ -NTs | 0.04 mA·cm ⁻² | 0.0013 | Diclofenac 5 mg/L, 80 mL | 62%–720 min | [40] |
| Ti ³⁺ /TiO ₂ | 0.10 mA·cm ⁻² | NA ^b | Diclofenac 5 mg/L, 80 mL | 100%–480 min | [41] |
| TiO ₂ -BiVO ₄ -BP/RP | NA | 0.0234 | Fluxapyroxa 10 mg/L, 100 mL | 96.5%–120 min | [42] |
| MI TiO ₂ , (111) NRs | NA | 0.032 | Dimethyl phthalate 2 mg/L, 50 mL | 88.3%–120 min | [43] |
| TNTs-Ag/SnO ₂ -Sb | 5.60 mA·cm ⁻² | NA | α -ethinylestradiol 1.2 mg/L, 100 mL | 60%–60 min | [44] |
| Au/TiO ₂ -NTs | 0.01 mA·cm ⁻² | 0.1560 | Methyl orange 5 mg/L, 100 mL | 56%–300 min | [11] |
| Ar-Fe ₂ O ₃ /Ti ³⁺ -TiO ₂ -NTs | 0.60 mA·cm ⁻² | 0.0684 | Tetracycline 20 mg/L, 100 mL | 100%–90 min | This work |

^a Rate constant.

^b NA: Not available.

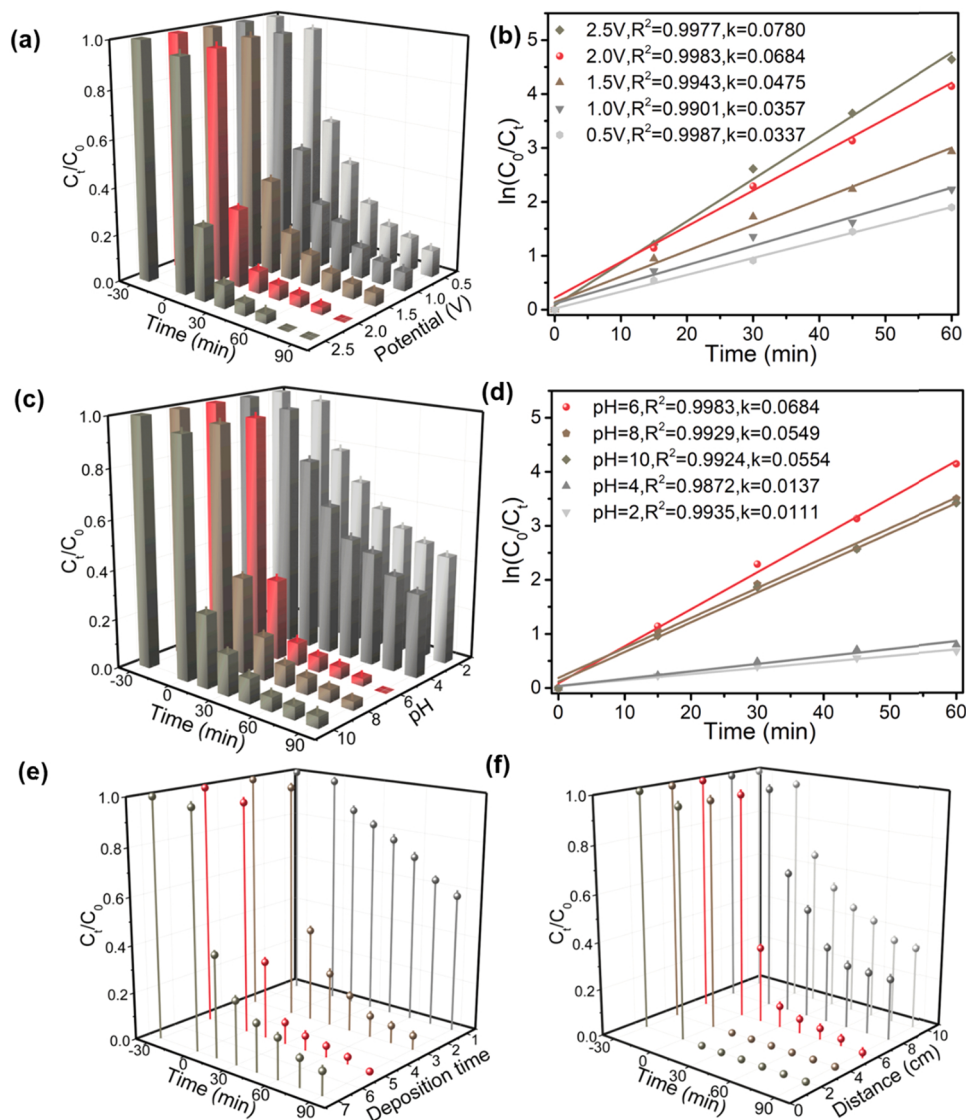


Fig. 7. Effect of (a) external potential on the PEC degradation and (b) degradation dynamics; Effect of (c) pH on the PEC degradation and (d) degradation dynamics; (e) Effect of deposition time; (f) Effect of photon flux.

Table 3

Photon flux corresponding to the distance between electrodes and light source.

| Distance/cm | 2 | 4 | 6 | 8 | 10 |
|---------------------------------|-------|-------|-------|-------|-------|
| Photon flux/mW·cm ⁻² | 466.7 | 403.6 | 318.2 | 291.9 | 243.1 |

Fig. 8d examined the performance of the photoelectrode from the perspective of mineralization ability. The mineralization efficiency of TC reached 60.05% within 90 min by Ar-Fe₂O₃/Ti³⁺-TiO₂-NTs. Meanwhile, **Fig. 8e** compared the treatment capacity of Ar-Fe₂O₃/Ti³⁺-TiO₂-NTs for different organic pollutants (Rhodamine B, Chlortetracycline, Doxycycline, Oxytetracycline, Norfloxacin, Levofloxacin and Metronidazole), and the degradation efficiency of all organic pollutants reached more than 95% within 90 min. Finally, the influence of different anions (Cl⁻, CO₃²⁻, PO₄³⁻) was displayed in **Fig. 8f**. The three anions within the concentration range of 5–20 mmol·L⁻¹ would not affect the degradation efficiency of TC, demonstrating the strong anti-interference ability of Ar-Fe₂O₃/Ti³⁺-TiO₂-NTs photoelectrode.

3.5. Catalytic mechanism analysis

In order to analyze the possible degradation mechanism of TC, the main active species needed to be determined firstly by free radical quenching experiments. •OH, ¹O₂, •O₂⁻ and h⁺ were captured by four free radical scavengers TBA, SA, BQ and EDTA-2Na, respectively. The experimental results suggested that the effect of excessive TBA and SA on TC degradation in the photoelectrocatalytic system was negligible. While after adding BQ and EDTA-2Na, the degradation efficiency of TC was obviously inhibited, especially in BQ, the efficiency was dropped from 100% to 51.81% (**Fig. 9a** and b). Therefore, the degradation of TC by the thin film electrode mainly depended on •O₂⁻ and h⁺ rather than •OH and ¹O₂, which was consistent with the judgement of voltage influence (**Fig. 7a**). The results of the capture experiment were examined by Electron paramagnetic resonance (EPR) (**Fig. 9c** and d). For DMPQ-•O₂⁻, there was no significant peak in the absence of light introduction. As the illumination time increased, the characteristic peak became more obvious. Nevertheless, the signal with a peak intensity of 1:1:1 gradually weakened with the increase of illumination time for TEMPO-h⁺. The characteristics of the above-mentioned characteristic peaks proved the

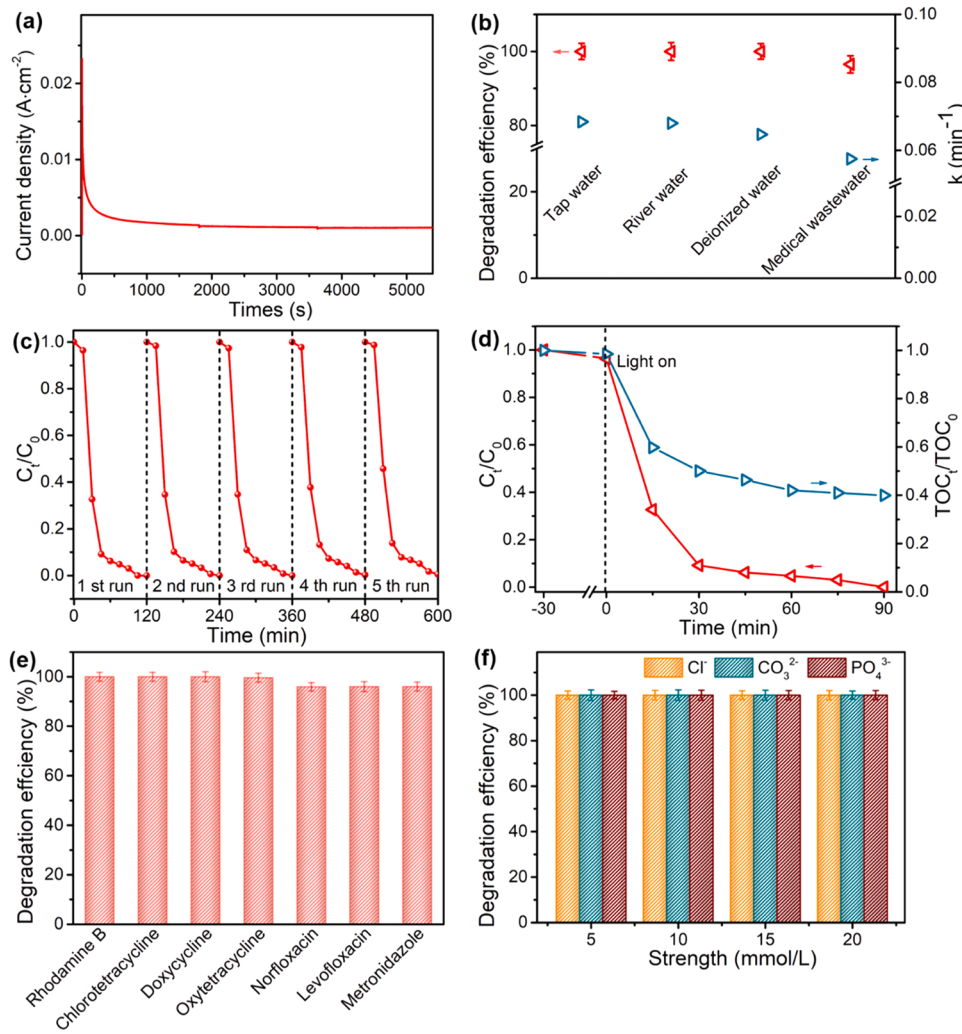


Fig. 8. (a) Long-time photocurrent decay curve; (b) TC degradation by Ar-Fe₂O₃/Ti³⁺-TiO₂-NTs photoelectrode in actual water samples; (c) Five cycles of degradation of TC by Ar-Fe₂O₃/Ti³⁺-TiO₂-NTs photoelectrode; (d) The degradation and TOC removal curves of TC on Ar-Fe₂O₃/Ti³⁺-TiO₂-NTs photoelectrode. (e) Catalytic degradation of various organic pollutants by Ar-Fe₂O₃/Ti³⁺-TiO₂-NTs photoelectrode; (f) Effect of ionic strength on the TC degradation. (Experimental conditions: initial pollutant concentration=20 mg·L⁻¹; V=100 mL).

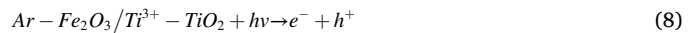
existence of $\bullet\text{O}_2^-$ and h^+ active species in the degradation system.

For clarifying the production pathway of active species, the energy band structure of photoelectrode was estimated. According to the Tauc plots, the band gap values of Ar-Fe₂O₃ and Ti³⁺-TiO₂ were estimated to be 2.19 and 2.80 eV, respectively (Fig. S7a and b). Then, the XPS valence band (VB) of Ar-Fe₂O₃ (2.50 eV) and Ti³⁺-TiO₂ (1.87 eV) were displayed in Fig. S7c. Combining with Eq. (7), the CB potentials of Ar-Fe₂O₃ and Ti³⁺-TiO₂ were calculated to -0.33 eV and -0.30 eV, and the detailed energy band structure was shown in Fig. S7d. Subsequently, the above energy level structure was verified by the flat band potential (U_{fb}) estimation. According to the x-intercept in the M-S diagrams, the U_{fb} of Ar-Fe₂O₃ and Ti³⁺-TiO₂ were -0.36 V and -0.38 V vs Ag/AgCl, respectively, which were equal to -0.163 V and -0.183 V vs NHE (Fig. S7e and f). The energy band calculation above was valid by virtue of the principle that the CB of n-type semiconductors is usually 0–0.2 V lower than that of U_{fb} [50].

$$E_{CB} = E_{VB} - E_g \quad (7)$$

Depending on the determination of active species and the analysis of energy band structure, the possible photo-electrocatalytic degradation mechanism was suggested (Scheme 2). Benefiting from the effective avoidance of light loss by unique nanotubes and the enhancement of visible-light harvesting ability after Ti³⁺ self-doping, the Ar-Fe₂O₃/Ti³⁺-TiO₂-NTs photoelectrode generated a large number of photogenerated e^- - h^+ (Eq. (8)). Based on the characteristics of the type II heterojunction between Ar-Fe₂O₃ and Ti³⁺-TiO₂ [14], the e^- in the CB of Ar-Fe₂O₃ could

migrate to the CB of Ti³⁺-TiO₂, which further being transferred to the external circuit, thereby achieving the effective separation of e^- - h^+ pairs. Since the CB potential of Ar-Fe₂O₃/Ti³⁺-TiO₂ were more negative than the oxidation potential of $\text{O}_2/\bullet\text{O}_2^-$ ($\text{O}_2/\bullet\text{O}_2^- = -0.28$ eV), and the Ar-Fe₂O₃ derived from MIL-100(Fe) gave the photoelectrode enhanced adsorption capacity, O_2 around the photoelectrode could be effectively captured to generate $\bullet\text{O}_2^-$ (Eq. (9)) [51]. Notably, the VB potential of Ti³⁺-TiO₂ was more positive than the standard reduction potential of $\bullet\text{OH}/\text{H}_2\text{O}$ (2.27 eV), so the oxidation of water by h^+ might occur to produce $\bullet\text{OH}$ (Eq. (10)). However, since the pH of the system was acidic, which was not conducive to the progress of Eq. (10), so the system tended to directly oxidize TC degradation by h^+ . In short, $\bullet\text{O}_2^-$ played the most important role in PEC degradation. Except for small part of h^+ for water oxidation, most of h^+ contributed to the degradation of TC (Eq. (11)), which was also corresponded to the capture experiment results.



3.6. Degradation pathway of TC by Ar-Fe₂O₃/Ti³⁺-TiO₂-NTs

The mass spectra of seven intermediates were identified based on the

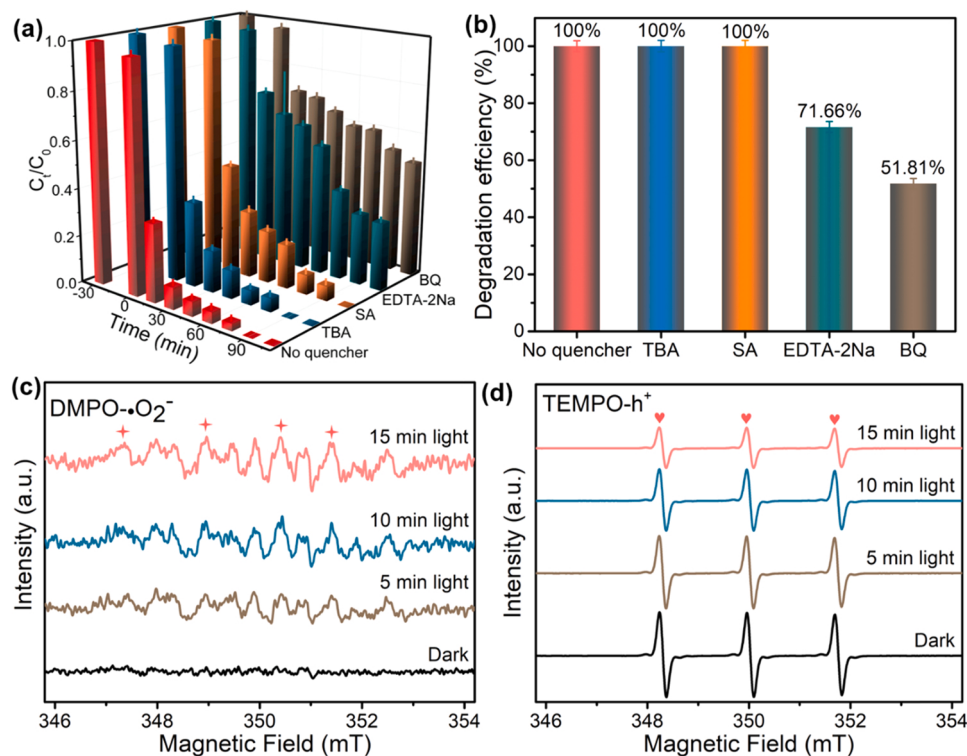
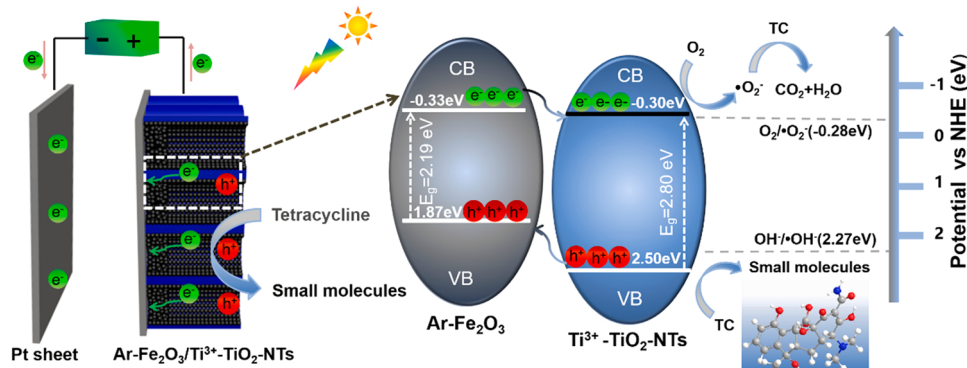


Fig. 9. (a, b) Effects of different radical scavengers on degradation of TC by Ar-Fe₂O₃/Ti³⁺-TiO₂-NTs photoelectrode; (c) EPR spectra of DMPO-•O₂⁻ adduct; (d) the spectra of TEMPO trapping photogenerated h⁺ for Ar-Fe₂O₃/Ti³⁺-TiO₂-NTs photoelectrode under visible light irradiation ($\lambda > 420$ nm).



Scheme 2. Proposed mechanism diagrams in Ar-Fe₂O₃/Ti³⁺-TiO₂-NTs.

fragment spectra obtained by liquid chromatography-mass spectrometry (LC-MS) (Fig. S8 and S9). The molecular weights and proposed molecular structures of the intermediates were summarized in Tab. S3. The peak with a retention time of 4.520 min corresponded to the TC molecule [52]. Compared with the original solution, the peak intensity of the TC molecule disappeared after the reaction (Fig. S10), which was consistent with the HPLC analysis (Fig. S4). Based on the attack mechanism and intermediates, the degradation pathways were suggested (Fig. 10). Firstly, TC was attacked by •O₂⁻ and h⁺, product P1 ($m/z = 418$) was resulted from the demethylation reaction at C4 due to lower N-C bond energy, which also reported in other studies [53]. After further dehydration and substitution of acylamino by carbinol group at C2, product P2 ($m/z = 393$) was obtained. As the reaction proceeds, the carbinol group was broken to generate the product P3 ($m/z = 362$). Product P4 ($m/z = 317$) was produced after the benzene rings of product P3 was cleavage, and under the continuous attack of •O₂⁻ and h⁺, product P5 ($m/z = 301$) and product P6 ($m/z = 284$) were obtained. After the dehydroxymethylation, product P7 ($m/z = 247$) was formed,

and then eventually oxidized into small molecules, even CO₂ and H₂O. According to the above analysis, the main products come from the dehydration, the cleavage of the benzene ring and the loss of certain groups (such as N-methyl, carboxyl). Notably, no hydroxylation products of TC, such as intermediate products with a typical molecular weight of $m/z = 461$ [54], were found in this study, which indicated that the role of •OH in the photo-electrocatalytic system was ignorable, which was consistent with the capture experiment.

4. Conclusion

In this research, the self-doping of Ti³⁺ on TiO₂-NTs was realized by electrochemical reduction. Then, MIL-100 (Fe) was successfully self-assembled on the basis of electrodeposited Fe, and a newly developed Ar-Fe₂O₃/Ti³⁺-TiO₂ photoelectrode was prepared by simple sculpture-reduction processes for TC degradation. Beneficial from the high conductivity/narrow band gap brought by Ti³⁺ self-doping, the uniform dispersion of Fe metal centers, the enhanced compactness/high mass

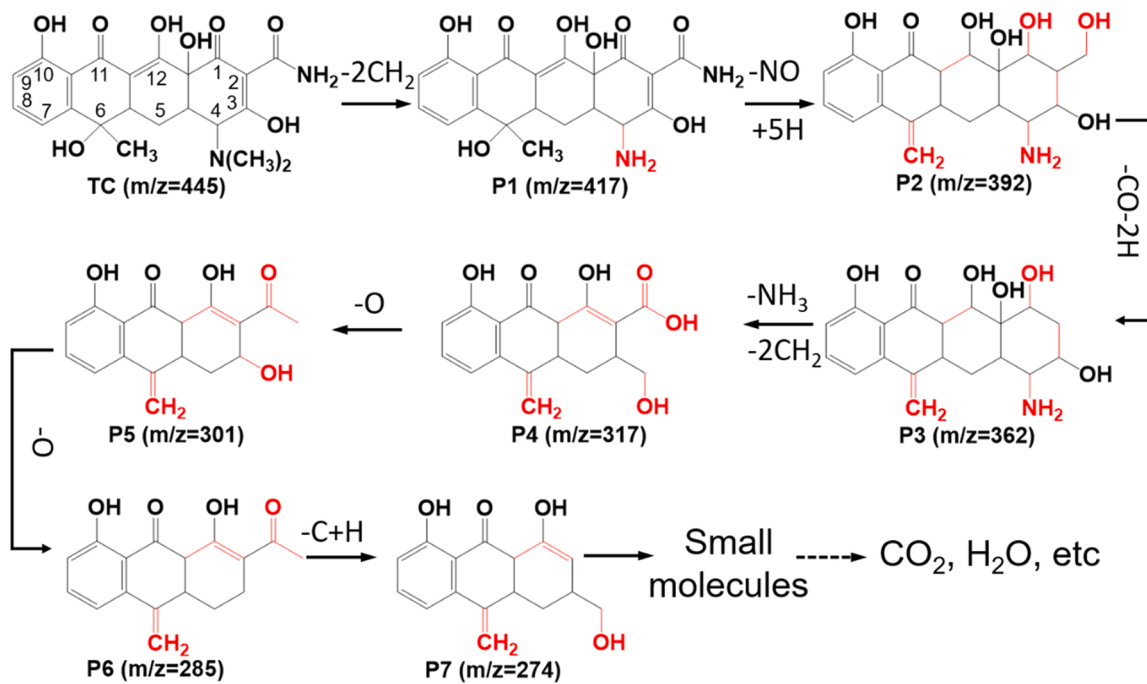


Fig. 10. Proposed TC pathway by the $\text{Ar-Fe}_2\text{O}_3/\text{Ti}^{3+}\text{-TiO}_2\text{-NTs}$ photoelectrode.

transfer efficiency caused by the self-assembly of MOFs, and the high separation rate of carriers formed by hybridization, the $\text{Ar-Fe}_2\text{O}_3/\text{Ti}^{3+}\text{-TiO}_2\text{-NTs}$ photoelectrode could achieve 100% degradation of TC within 90 min. Based on the heterojunction inside the photoelectrode and the auxiliary external circuit, as well as suitable conduction band level, the photogenerated e^- and h^+ were effectively separated to oxidize O_2 to $\bullet\text{O}_2^-$ indirectly degrading and directly degrading pollutants, respectively. Finally, quenching experiments and ESR detection revealed that $\bullet\text{O}_2^-$ and h^+ were responsible for the oxidation of TC. This work provided a general strategy for electrochemical modification of $\text{TiO}_2\text{-NTs}$ and in-situ self-assembly of MOFs, and advanced the MOFs photoelectrodes-based oxidation technology toward refractory organic pollutants degradation.

CRediT authorship contribution statement

Meiyng Jia: Conceptualization, Methodology, Writing – original draft preparation. **Qi Liu:** Methodology, Data curation. **Weiping Xiong:** Investigation, Project administration, Writing – review & editing. **Zhaohui Yang:** Supervision, Resources, Writing – review & editing. **Chang Zhang:** Supervision, Writing-Reviewing and editing. **Dongbo Wang:** Supervision, Writing – review & editing. **Yinping Xiang:** Writing – review & editing. **Haihao Peng:** Visualization, Writing – review & editing. **Jing Tong:** Writing – review & editing. **Jiao Cao:** Visualization, Writing – review & editing. **Haiyin Xu:** Writing – review & editing.

Declaration of Competing Interest

The authors declare that they have no known competing financial interests or personal relationships that could have appeared to influence the work reported in this paper.

Acknowledgements

The work was supported by the National Natural Science Foundation of China [grant no. 51878258]; the National Youth Foundation of China [grant no. 52000064]; Changsha Municipal Natural Science Foundation [grant no. kq2014054]; the Special Funds for the Construction of

Innovative Provinces in Hunan [grant no. 2021SK2040]; the Science and Technology Innovation Program of Hunan Province [2021RC2100] and the Science and Technology Innovation Program of Hunan Province [grant no. 2021RC3133]. The authors would like to thank Yecheng Fan from Shidianjia Lab (www.shidianjia.com) for the EPR analysis.

Appendix A. Supporting information

Supplementary data associated with this article can be found in the online version at [doi:10.1016/j.apcatb.2022.121344](https://doi.org/10.1016/j.apcatb.2022.121344).

References

- [1] J. Qiu, W. Zheng, R. Yuan, C. Yue, D. Li, F. Liu, J. Zhu, A novel 3D nanofibrous aerogel-based $\text{MoS}_2@\text{Co}_3\text{S}_4$ heterojunction photocatalyst for water remediation and hydrogen evolution under simulated solar irradiation, *Appl. Catal. B* 264 (2020) 118514–118525.
- [2] C. Wang, J. Luan, C. Wu, Metal-organic frameworks for aquatic arsenic removal, *Water Res.* 158 (2019) 370–382.
- [3] J. Wang, C. Xue, W. Yao, J. Liu, X. Gao, R. Zong, Z. Yang, W. Jin, D. Tao, MOF-derived hollow $\text{TiO}_2@\text{C/FeTiO}_3$ nanoparticles as photoanodes with enhanced full spectrum light PEC activities, *Appl. Catal. B* 250 (2019) 369–381.
- [4] W. Dai, Y. Tao, H. Zou, S. Xiao, G. Li, D. Zhang, H. Li, Gas-phase photoelectrocatalytic oxidation of NO via TiO_2 nanorod array/FTO photoanodes, *Environ. Sci. Technol.* 54 (2020) 5902–5912.
- [5] Y. Xie, L. Zhou, C. Huang, H. Huang, J. Lu, Fabrication of nickel oxide-embedded titania nanotube array for redox capacitance application, *Electrochim. Acta* 53 (2008) 3643–3649.
- [6] H. Zhang, J.H. Kim, J.H. Kim, J.S. Lee, Engineering highly ordered iron titanate nanotube array photoanodes for enhanced solar water splitting activity, *Adv. Funct. Mater.* 27 (2017) 35–43.
- [7] K. Cho, S. Lee, H. Kim, H.-E. Kim, A. Son, E.-j Kim, M. Li, Z. Qiang, S.W. Hong, Effects of reactive oxidants generation and capacitance on photoelectrochemical water disinfection with self-doped titanium dioxide nanotube arrays, *Appl. Catal. B* 257 (2019) 117910–117918.
- [8] X.L. Yang hou, Qidong Zhao, Xie Quan, Guohua Chen, Electrochemically assisted photocatalytic degradation of 4-chlorophenol by ZnFe_2O_4 -modified TiO_2 nanotube array electrode under visible light irradiation, *Environ. Sci. Technol.* 44 (2010) 5098–5103.
- [9] R. Tang, S. Zhou, L. Zhang, L. Yin, Metal-organic framework derived narrow bandgap cobalt carbide sensitized titanium dioxide nanocage for superior photoelectrochemical water oxidation performance, *Adv. Funct. Mater.* 28 (2018) 1706154–1706164.
- [10] H.-Y. Wang, R. Hu, N. Wang, G.-L. Hu, K. Wang, W.-H. Xie, R. Cao, Boosting photoanodic activity for water splitting in carbon dots aqueous solution without any traditional supporting electrolyte, *Appl. Catal. B* 296 (2021) 120378–120385.

[11] L. Wu, F. Li, Y. Xu, J.W. Zhang, D. Zhang, G. Li, H. Li, Plasmon-induced photoelectrocatalytic activity of Au nanoparticles enhanced TiO₂ nanotube arrays electrodes for environmental remediation, *Appl. Catal. B* 164 (2015) 217–224.

[12] Y. Hou, X. Li, Q. Zhao, G. Chen, C.L. Raston, Role of hydroxyl radicals and mechanism of Escherichia coli inactivation on Ag/AgBr/TiO₂ nanotube array electrode under visible light irradiation, *Environ. Sci. Technol.* 46 (2012) 4042–4050.

[13] M. Jia, Z. Yang, H. Xu, P. Song, W. Xiong, J. Cao, Y. Zhang, Y. Xiang, J. Hu, C. Zhou, Y. Yang, W. Wang, Integrating N and F co-doped TiO₂ nanotubes with ZIF-8 as photoelectrode for enhanced photo-electrocatalytic degradation of sulfamethazine, *Chem. Eng. J.* 388 (2020) 124388–124401.

[14] M. Jia, Z. Yang, W. Xiong, J. Cao, Y. Xiang, H. Peng, Y. Jing, C. Zhang, H. Xu, P. Song, Magnetic heterojunction of oxygen-deficient Ti³⁺-TiO₂ and Ar-Fe₂O₃ derived from metal-organic frameworks for efficient peroxydisulfate (PDS) photo-activation, *Appl. Catal. B* 298 (2021) 120513–120525.

[15] M. Jourshabani, M.R. Asrami, B.-K. Lee, An efficient and unique route for the fabrication of highly condensed oxygen-doped carbon nitride for the photodegradation of synchronous pollutants and H₂O₂ production under ambient conditions, *Appl. Catal. B* 302 (2022) 120839–120852.

[16] S.H. Williams, Effect of prohibition of the use of tetracyclines in animal feeds on tetracycline resistance of faecal *e. coli* of pigs, *Nature* 243 (1973) 237–238.

[17] Y. Zhou, C. Zhang, D. Huang, W. Wang, Y. Zhai, Q. Liang, Y. Yang, S. Tian, H. Luo, D. Qin, Structure defined 2D Mo₂C/2D g-C₃N₄ Van der Waals heterojunction: oriented charge flow in-plane and separation within the interface to collectively promote photocatalytic degradation of pharmaceutical and personal care products, *Appl. Catal. B* 301 (2022) 120749–120761.

[18] B. Wang, Y. Zhang, D. Zhu, H. Li, Assessment of bioavailability of biochar-sorbed tetracycline to escherichia coli for activation of antibiotic resistance genes, *Environ. Sci. Technol.* 54 (2020) 12920–12928.

[19] X. Liu, R. Dang, W. Dong, X. Huang, J. Tang, H. Gao, G. Wang, A sandwich-like heterostructure of TiO₂ nanosheets with MIL-100(Fe): a platform for efficient visible-light-driven photocatalysis, *Appl. Catal. B* 209 (2017) 506–513.

[20] W. Wu, J. Zhu, Y.H. Deng, Y. Xiang, Y.W. Tan, H.Q. Tang, H. Zou, Y.F. Xu, Y. Zhou, TiO₂ nanocrystals with the {001} and {101} facets co-exposed with MIL-100(Fe): an egg-like composite nanomaterial for efficient visible light-driven photocatalysis, *RSC Adv.* 9 (2019) 31728–31734.

[21] S. Tan, Z. Xing, J. Zhang, Z. Li, X. Wu, J. Cui, J. Kuang, Q. Zhu, W. Zhou, Ti³⁺-TiO₂/g-C₃N₄ mesostructured nanosheets heterojunctions as efficient visible-light-driven photocatalysts, *J. Catal.* 357 (2018) 90–99.

[22] J. Dong, J. Han, Y. Liu, A. Nakajima, S. Matsushita, S. Wei, W. Gao, Defective black TiO₂O synthesized via anodization for visible-light photocatalysis, *ACS Appl. Mater. Interfaces* 6 (2014) 1385–1388.

[23] H. Lv, H. Zhao, T. Cao, L. Qian, Y. Wang, G. Zhao, Efficient degradation of high concentration azo-dye wastewater by heterogeneous Fenton process with iron-based metal-organic framework, *J. Mol. Catal. A. Chem.* 400 (2015) 81–89.

[24] H. Tian, T. Araya, R. Li, Y. Fang, Y. Huang, Removal of MC-LR using the stable and efficient MIL-100/MIL-53(Fe) photocatalyst: the effect of coordinate immobilized layers, *Appl. Catal. B* 254 (2019) 371–379.

[25] S.K. Mohapatra, S. Banerjee, M. Misra, Synthesis of Fe₂O₃/TiO₂ nanorod-nanotube arrays by filling TiO₂ nanotubes with Fe, *Nanotechnology* 19 (2008) 315601–315608.

[26] Z. Guo, J.K. Cheng, Z. Hu, M. Zhang, Q. Xu, Z. Kang, D. Zhao, Metal-organic frameworks (MOFs) as precursors towards TiO₂/C composites for photodegradation of organic dye, *RSC Adv.* 4 (2014) 34221–34225.

[27] B. Sun, W. Zhou, H. Li, L. Ren, P. Qiao, F. Xiao, L. Wang, B. Jiang, H. Fu, Magnetic Fe₂O₃/mesoporous black TiO₂ hollow sphere heterojunctions with wide-spectrum response and magnetic separation, *Appl. Catal. B* 221 (2018) 235–242.

[28] M. Kulkarni, J. Šepitka, I. Junkar, M. Benčina, N. Rawat, A. Mazare, C. Rode, S. Gokhale, P. Schmuki, M. Daniel, A. Iglíč, Mechanical properties of anodic titanium dioxide nanostructures, *Mater. Tehnol.* 55 (2021) 19–24.

[29] W. Feng, L. Lin, H. Li, B. Chi, J. Pu, J. Li, Hydrogenated TiO₂/ZnO heterojunction nanorod arrays with enhanced performance for photoelectrochemical water splitting, *Int. J. Hydrog. Energy* 42 (2017) 3938–3946.

[30] Q. Wang, Y. Lei, Z. Chen, N. Wu, Y. Wang, B. Wang, Y. Wang, Fe/Fe₃C@C nanoparticles encapsulated in N-doped graphene-CNTs framework as an efficient bifunctional oxygen electrocatalyst for robust rechargeable Zn-air batteries, *J. Mater. Chem. B* 6 (2018) 516–526.

[31] P. Wu, C. Liu, Y. Luo, K. Wu, J. Wu, X. Guo, J. Hou, Z. Liu, A novel black TiO₂/ZnO nanocone arrays heterojunction on carbon cloth for highly efficient photoelectrochemical performance, *Front. Mater. Sci.* 13 (2019) 43–53.

[32] X. Hou, S.L. Stanley, M. Zhao, J. Zhang, H. Zhou, Y. Cai, F. Huang, Q. Wei, MOF-based C-doped coupled TiO₂/ZnO nanofibrous membrane with crossed network connection for enhanced photocatalytic activity, *J. Alloy. Compd.* 777 (2019) 982–990.

[33] L. Shen, Z. Xing, J. Zou, Z. Li, X. Wu, Y. Zhang, Q. Zhu, S. Yang, W. Zhou, Black TiO₂ nanobelts/g-C₃N₄ nanosheets laminated heterojunctions with efficient visible-light-driven photocatalytic performance, *Sci. Rep.* 7 (2017) 41978–41988.

[34] C. Zhang, M. Jia, Z. Xu, W. Xiong, Z. Yang, J. Cao, H. Peng, H. Xu, Y. Xiang, Y. Jing, Constructing 2D/2D N-ZnO/g-C₃N₄ S-scheme heterojunction: efficient photocatalytic performance for norfloxacin degradation, *Chem. Eng. J.* 430 (2022) 132652–132661.

[35] R.S. Schrebler, H. Altamirano, P. Grez, F.V. Herrera, E.C. Muñoz, L.A. Ballesteros, R.A. Córdova, H. Gómez, E.A. Dalchiele, The influence of different electrodeposition E/t programs on the photoelectrochemical properties of α -Fe₂O₃ thin films, *Thin Solid Films* 518 (2010) 6844–6852.

[36] C.L. Ricardo Schrebler, Francisca Vera, Paula Cury, Eduardo Muñoz, Rodrigo del Río, Humberto Gómez Meier, E.A.D. Ricardo Córdova, An electrochemical deposition route for obtaining-Fe₂O₃ thin films, *Electrochim. Solid State Lett.* 10 (2007) 95–99.

[37] G. Wang, H. Zhang, W. Wang, X. Zhang, Y. Zuo, Y. Tang, X. Zhao, Fabrication of Fe-TiO₂-NTs/SnO₂-Sb-Ce electrode for electrochemical degradation of aniline, *Sep. Purif. Technol.* 268 (2021) 118591–118600.

[38] C. Zhou, C. Lai, P. Xu, G. Zeng, D. Huang, C. Zhang, M. Cheng, L. Hu, J. Wan, Y. Liu, W. Xiong, Y. Deng, M. Wen, In situ grown AgI/Bi₂O_{1.7}Cl₂ heterojunction photocatalysts for visible light degradation of sulfamethazine: efficiency, pathway, and mechanism, *ACS Sustain. Chem. Eng.* 6 (2018) 4174–4184.

[39] X. Deng, H. Zhang, R. Guo, X. Cheng, Q. Cheng, Construction of AgBr nano-cakes decorated Ti³⁺-self-doped TiO₂ nanorods/nanosheets photoelectrode and its enhanced visible light driven photocatalytic and photoelectrochemical properties, *Appl. Surf. Sci.* 441 (2018) 420–428.

[40] X. Cheng, H. Liu, Q. Chen, J. Li, P. Wang, Enhanced photoelectrocatalytic performance for degradation of diclofenac and mechanism with TiO₂ nanoparticles decorated TiO₂ nano-tubes arrays photoelectrode, *Electrochim. Acta* 108 (2013) 203–210.

[41] X. Cheng, Q. Cheng, X. Deng, P. Wang, H. Liu, A facile and novel strategy to synthesize reduced TiO₂ nanotubes photoelectrode for photoelectrocatalytic degradation of diclofenac, *Chemosphere* 144 (2016) 888–894.

[42] Y. Wang, J. Wu, Y. Yan, L. Li, P. Lu, J. Guan, N. Lu, X. Yuan, Black phosphorus-based semiconductor multi-heterojunction TiO₂-BiVO₄-BP/RP film with an in situ junction and Z-scheme system for enhanced photoelectrocatalytic activity, *Chem. Eng. J.* 403 (2021) 121613–121621.

[43] J. Zhang, B. Tang, G. Zhao, Selective photoelectrocatalytic removal of dimethyl phthalate on high-quality expressed molecular imprints decorated specific facet of single crystalline TiO₂ photoanode, *Appl. Catal. B* 279 (2020) 119364–119371.

[44] H. He, S. Sun, J. Gao, B. Huang, T. Zhao, H. Deng, X. Wang, X. Pan, Photoelectrocatalytic simultaneous removal of 17alpha-ethinylestradiol and E. coli using the anode of Ag and SnO₂-Sb 3D-loaded TiO₂ nanotube arrays, *J. Hazard. Mater.* 398 (2020) 122805–122814.

[45] M. Xu, Y. Mao, W. Song, X. OuYang, Y. Hu, Y. Wei, C. Zhu, W. Fang, B. Shao, R. Lu, F. Wang, Preparation and characterization of Fe-Ce co-doped Ti/TiO₂ NTs/PbO₂ nanocomposite electrodes for efficient electrocatalytic degradation of organic pollutants, *J. Electroanal. Chem.* 823 (2018) 193–202.

[46] H. Peng, W. Xiong, Z. Yang, J. Cao, M. Jia, Y. Xiang, Q. Hu, Z. Xu, Facile fabrication of three-dimensional hierarchical porous ZIF-L/gelatin aerogel: highly efficient adsorbent with excellent recyclability towards antibiotics, *Chem. Eng. J.* 426 (2021) 130798–130807.

[47] Q. Hu, J. Cao, Z. Yang, W. Xiong, Z. Xu, P. Song, M. Jia, Y. Zhang, H. Peng, A. Wu, Fabrication of Fe-doped cobalt zeolitic imidazolate framework derived from Co (OH)₂ for degradation of tetracycline via peroxymonosulfate activation, *Sep. Purif. Technol.* 259 (2021) 118059–118068.

[48] J. Chen, Y. Xia, Q. Dai, Electrochemical degradation of chloramphenicol with a novel Al doped PbO₂ electrode: performance, kinetics and degradation mechanism, *Electrochim. Acta* 165 (2015) 277–287.

[49] J. Zheng, K. Huang, G. Hou, H. Zhang, H. Cao, A highly active Pt nanocatalysts supported on RuO₂ modified TiO₂-NTs for methanol electrooxidation with excellent CO tolerance, *Int. J. Hydrog. Energy* 44 (2019) 31506–31514.

[50] C. Feng, Y. Deng, L. Tang, G. Zeng, J. Wang, J. Yu, Y. Liu, B. Peng, H. Feng, J. Wang, Core-shell Ag₂CrO₄/N-QDs@g-C₃N₄ composites with anti-phtocorrosion performance for enhanced full-spectrum-light photocatalytic activities, *Appl. Catal. B* 239 (2018) 525–536.

[51] Q. Tang, X. An, H. Lan, H. Liu, J. Qu, Polyoxometalates/TiO₂ photocatalysts with engineered facets for enhanced degradation of bisphenol A through persulfate activation, *Appl. Catal. B* 268 (2020), 118394–111402.

[52] J. Cao, Z. Yang, W. Xiong, Y. Zhou, Y. Wu, M. Jia, H. Peng, Y. Yuan, Y. Xiang, C. Zhou, Three-dimensional MOF-derived hierarchically porous aerogels activate peroxymonosulfate for efficient organic pollutants removal, *Chem. Eng. J.* 427 (2022) 427–527.

[53] H. Dong, Z. Jiang, C. Zhang, J. Deng, K. Hou, Y. Cheng, L. Zhang, G. Zeng, Removal of tetracycline by Fe/Ni bimetallic nanoparticles in aqueous solution, *J. Colloid Interface Sci.* 513 (2018) 117–125.

[54] S. He, C. Yan, X.-Z. Chen, Z. Wang, T. Ouyang, M.-L. Guo, Z.-Q. Liu, Construction of core-shell heterojunction regulating α -Fe₂O₃ layer on CeO₂ nanotube arrays enables highly efficient Z-scheme photoelectrocatalysis, *Appl. Catal. B* 276 (2020) 119138–119148.